

Geometry by Deflaring

Fima Koreban and Yoav Y. Schechner

Department of Electrical Engineering

Technion – Israel Institute of Technology, Haifa 32000, Israel

fima@tx.technion.ac.il, yoav@ee.technion.ac.il

Abstract

Stray light reflected by lens surfaces creates flare which affects the image. A pronounced form of this flare is aperture ghosting, where bright spots that resemble the shape of the lens aperture are overlayed on the image. This might disrupt image analysis. It occurs when a bright narrow source (usually the Sun) is in the vicinity of the field of view, though often the source may be outside the actual viewed field. This paper analyzes the geometry of this phenomenon. It theoretically proves empirical observations, particularly the condensation of this flare around a straight line. Based on the image-formation model, we devise a very simple method for mitigating this effect, using as few as two frames taken when the camera moves. This significantly improves the images. Furthermore, aperture ghosting is shown to encode useful geometric information, specifically the location of the (often unseen) illumination source, and the optical center of the camera. Hence, our approach decodes this information as a by-product of deflaring. This is demonstrated experimentally outdoors.

1. Introduction

The image irradiance may not represent well the object radiance at the corresponding location. One reason is that part of the light emanating from the scene undergoes reflections between components in the lens system [13], becoming *stray light*. This light affects unintended locations in the image plane, thus biasing the intensity readout in these locations. This phenomenon is known as *lens flare* or *veiling glare* [9, 12, 13, 18, 15]. Flare is sometimes added intentionally as a special effect [8].

Stray light may originate from sources outside (but close to) the field of view (FOV): the source does not project into the CCD area, but still shines into the lens and creates the effect. Most objects do not create stray light of appreciable energy. The effect, however, is significant if the scene in front has a very bright light source, while some objects in view are dim. The effect is particularly disturbing if the bright light source is narrow: then the flare pattern is strongly spatially varying, as seen in Fig. 1. This may inhibit understanding of underlying objects. It may even saturate the image. Furthermore, this additive component increases photon noise [19]. This form of flare is termed *aperture ghosting* [24], as it resembles scaled replicas of



Figure 1. Aperture ghosting: bright spots resembling the aperture (nearly hexagonal here). Photo courtesy of Paul van Walree [21].

the lens aperture, e.g., hexagonals.

This paper analyzes the formation of aperture ghosting. It yields radiometric and geometric models of the problem. The analysis shows that flare may actually be *good for vision*. Aperture-ghosting *encodes information* about the scene and the camera. Hence, a method that can isolate flare can extract this information. The analysis explains analytically the locality of aperture ghosts (Fig. 1) and their geometry. Based on this, we propose a very simple approach that effectively counters the ghosting.

Effective glare-removal systems were proposed in Refs. [12, 18]. The method in [12] requires insertion of a special mask into the camera, and involves a significant loss of spatial resolution. Ref. [18] requires a significant number of raw frames taken by a static camera. There, imaging is done through a mask which should be in approximate focus with the scene. Light is lost in opaque areas of the mask. In contrast, the approach described here is fast and works with as few as two frames. It requires no special hardware, and no light loss. It is thus easily demonstrated in outdoor experiments. Note that flare may also be treated by image deconvolution [18]. However, deconvolution is difficult if the main source of the problem (the Sun) is not captured, being outside either the FOV or the camera's dynamic range.

The approach we use works with camera motion. This enables its use in a wide range of applications. As a by-product, our approach exploits the flare to extract additional information. Specifically, it estimates the location of the illumination source (which is often outside the FOV), and the projection of the optical center of the camera.

2. Theoretical Background

A compound camera lens typically contains several refractive optical elements and an iris. As a light ray \mathcal{L} enters the lens and propagates in the system, this ray encounters air-glass interfaces. In each such interface, a portion of the ray's energy is reflected. Light which is reflected outwards from one inner interface may be back-reflected into the camera chamber by another interface. Hence, a set of secondary reflected light rays $\{\tilde{\mathcal{L}}_q\}_{q=1}^{N_{\text{secondary}}}$ is created.

In computer vision, other separation problems involved secondary reflections. The reflections were not modeled in the lens, but within the scene. Ref. [14] modeled lighting with increasing orders of rays reflected from the surroundings. Ref. [4] modeled secondary semireflections in a window, and proposed a deghosting method for them.

In our case, the secondary rays are created in the lens and propagate to the image plane. Usually, at each lens surface, a ray \mathcal{L} hits the curved lens interfaces at an angle. Hence, the reflection deviates the ray direction. This causes the secondary rays $\{\tilde{\mathcal{L}}_q\}$ to spatially deviate from \mathcal{L} . Hence, light which was supposed to arrive at a certain pixel (if no reflections occurred) is distributed over a set of different locations. This causes flare.

The number $N_{\text{secondary}}$ can be quite large, even for simple systems. Suppose there are n_{lens} optical element-groups.¹ They have $2n_{\text{lens}}$ air-glass interfaces. Based on Refs. [13, 18], the total number of secondary reflections is $N_{\text{secondary}} = 2n_{\text{lens}}^2 - n_{\text{lens}}$. For example, in a rather basic but common Tessar system, which has three element groups, 15 secondary reflections are caused by the lenses. Also, the CCD chip may reflect toward the lenses light, which is then backreflected. As a result, it can be shown that we get

$$N_{\text{secondary}} = 2n_{\text{lens}}^2 + n_{\text{lens}} . \quad (1)$$

Stray light is reduced by anti-reflection coatings over the glass interfaces [13], and by use of baffles [15]. Coatings decrease reflection [11] from glass to $\approx 0.3\%$, down from $\approx 4\%$ of uncoated interfaces. Reflection from two coated surfaces thus channels $\approx \mathcal{O}(10^{-5})$ of the energy of \mathcal{L} to each secondary (flare creating) ray $\tilde{\mathcal{L}}_q$. This is very low for most objects in the scene. However, it is not sufficiently low when a strong light source, such as the Sun or a lamp shines light directly into the lens. Take the typical value [5] that the radiance of such illumination sources is $\mathcal{O}(10^5 - 10^6)$ brighter than the rest of the scene. Then, flare may appear as bright as the imaged objects.

¹An element group is either a single optical element, or multiple elements that are glued together such that there is no air between them.

3. Image Formation model

3.1. Photometry

The coordinate of a pixel is $\mathbf{x} = (x, y)$, in the local coordinate system of a frame. Had there been no reflections in the camera system, the image irradiance would have been $i(\mathbf{x})$. Reflections inside the camera create two effects. First, energy carried by the main beam towards an intended pixel is decreased, since this energy is reflected elsewhere. Overall, the transmittance of the lens system is decreased to $T < 1$. If all the air-glass interfaces have reflectance R , then, $T = (1 - R)^{2n_{\text{lens}}}$. Second, portion of the reflected energy appears as an additive flare $F(\mathbf{x})$, where $F(\mathbf{x}) \geq 0$. Overall, the measured image irradiance is

$$G(\mathbf{x}) = I(\mathbf{x}) + F(\mathbf{x}) , \quad (2)$$

where $I(\mathbf{x}) = Ti(\mathbf{x})$.

The transmittance T is independent of the scene, and is a fixed function of the lens hardware. Hence, T can be estimated or calibrated beforehand, and then be compensated for in any new image. Thus, in this paper we are not interested in such a fixed compensation. We aim to separate $I(\mathbf{x})$ from $F(\mathbf{x})$, both of which are scene dependent.

3.2. Geometry

This section derives a theoretical geometric model for aperture ghosting. The optical axis (OA) is a straight line, which is the axis of radial symmetry of the system.² A world point has a three dimensional (3D) coordinate vector \mathbf{X} . The camera has a center of projection at $\mathbf{X}^{\text{center}} \in \text{OA}$. Let the scene be illuminated by an off-axis single bright point source, such as the Sun. Its position in the world coordinates is \mathbf{X}^{sol} .

Consider Fig. 2. One plane in space, denoted by $\mathcal{P}^{\text{meridion}}$ includes both the OA and the off-axis point \mathbf{X}^{sol} :

$$\text{OA}, \mathbf{X}^{\text{sol}} \in \mathcal{P}^{\text{meridion}} . \quad (3)$$

This is the *meridional* (tangential) plane [6] with respect to \mathbf{X}^{sol} . The *chief ray* [6], denoted as \mathcal{C} , emanates from \mathbf{X}^{sol} and enters the lens system at $\mathbf{X}^{\text{center}} \in \text{OA}$. As $\mathbf{X}^{\text{center}}, \mathbf{X}^{\text{sol}} \in \mathcal{C}$, following Eq. (3)

$$\mathcal{C} \in \mathcal{P}^{\text{meridion}} . \quad (4)$$

Let a point in the lens system be parameterized by (ρ, ϕ, z) , where z is the coordinate on the OA, ρ is the distance from the OA, and ϕ is the azimuth. The plane $\mathcal{P}^{\text{meridion}}$ has a fixed ϕ . At all the lens interfaces, the surface normal has no azimuthal component, as the lens has radial symmetry around the OA. After it enters the lens, the ray \mathcal{C} propagates through the system and refracts. It also

²Radial symmetry exists if the optical system is aligned. Then, all its elements are positioned such that they are centered and oriented on a shared OA. The iris is typically not circular. Nevertheless, it is symmetric and its center resides on the OA.

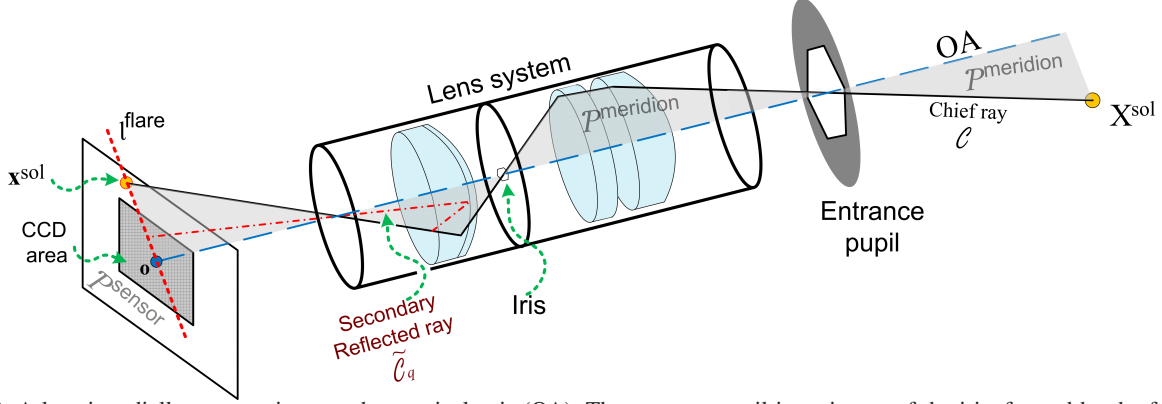


Figure 2. A lens is radially symmetric around an optical axis (OA). The entrance pupil is an image of the iris, formed by the front lens elements. Light is projected to $\mathcal{P}^{\text{sensor}}$, in which the CCD array resides. Jointly with the OA, the chief ray \mathcal{C} from the light source at \mathbf{X}^{sol} defines the meridional plane $\mathcal{P}^{\text{meridion}}$. Secondary reflected rays $\{\tilde{\mathcal{C}}_q\}$ created by \mathcal{C} are confined to $\mathcal{P}^{\text{meridion}}$, and create flare in the form of aperture ghosting. It condenses on line ℓ^{flare} . This line passes through \mathbf{x}^{sol} and \mathbf{o} , i.e., the respective projections of \mathbf{X}^{sol} and the OA.

generates a set of internally reflected rays $\{\tilde{\mathcal{C}}_q\}_{q=1}^{N_{\text{secondary}}}$. Since the refracting/reflective interfaces have no azimuthal inclination, the chief ray \mathcal{C} maintains a fixed ϕ and thus cannot leave $\mathcal{P}^{\text{meridion}}$. For the same reason, also the *reflected rays (generated by \mathcal{C}) are constrained to this plane*, i.e.,

$$\{\tilde{\mathcal{C}}_q\}_{q=1}^{N_{\text{secondary}}} \in \mathcal{P}^{\text{meridion}}, \quad (5)$$

as illustrated in Fig. 2.

Denote the image plane as $\mathcal{P}^{\text{sensor}}$, i.e. $\text{CCD} \subset \mathcal{P}^{\text{sensor}}$. This plane is intersected by the OA at

$$\mathbf{o} = \mathcal{P}^{\text{sensor}} \cap \text{OA}, \quad (6)$$

which is defined here as the *optical center* of the image frame. The projection of \mathbf{X}^{sol} on the sensor plane is at

$$\mathbf{x}^{\text{sol}} = \mathcal{P}^{\text{sensor}} \cap \mathcal{C}. \quad (7)$$

Often, \mathbf{x}^{sol} is outside the camera FOV, i.e., the Sun's projected image lies outside the area occupied by the CCD.

The planes $\mathcal{P}^{\text{sensor}}$ and $\mathcal{P}^{\text{meridion}}$ intersect at a straight line,

$$\ell^{\text{flare}} = \mathcal{P}^{\text{sensor}} \cap \mathcal{P}^{\text{meridion}}. \quad (8)$$

Considering Fig. 2, this line has the following properties:

- It represents a line in the image data, since $\ell^{\text{flare}} \subset \mathcal{P}^{\text{sensor}}$.
- It is a radial line in the image: ℓ^{flare} passes through \mathbf{o} . This follows from Eqs. (3,6), which dictate that \mathbf{o} lies at the intersection expressed in Eq. (8).
- The point \mathbf{x}^{sol} resides on ℓ^{flare} . This follows from Eqs. (3,7), which dictate that \mathbf{x}^{sol} lies at the intersection expressed in Eq. (8).

For the moment, let the lens iris be closed almost completely, such that the system functions similarly to a pinhole camera, geometrically. Then, only the chief ray exists. Hence, the only secondary reflected rays originating from the Sun are the set $\{\tilde{\mathcal{C}}_q\}$. These reflected rays hit $\mathcal{P}^{\text{sensor}}$ at a set of locations

$$\Phi_{\mathcal{C}} = \{\tilde{\mathcal{C}}_q\} \cap \mathcal{P}^{\text{sensor}}. \quad (9)$$

This is the set of points in the image plane that have lens flare³ originating from \mathbf{X}^{sol} . Using Eqs. (5,9) in Eq. (8), it follows that $\Phi_{\mathcal{C}} \in \ell^{\text{flare}}$, i.e., the flare's *aperture ghosts* all reside on the line ℓ^{flare} . To conclude, the following theorem applies to well-aligned cameras:

Theorem 1: *If the iris is nearly closed, flare is limited to a straight line in the image. This line passes through the frame's optical center \mathbf{o} and the Sun's image location \mathbf{x}^{sol} .*

Since a radial line is invariant to radial distortions, it is straightforward to prove the following:

Corollary 2: *The line ℓ^{flare} is invariant to radial geometric distortions and their corrections.*

However, $\Phi_{\mathcal{C}}$ is distorted, since it can move and change within ℓ^{flare} . Generalization of the analysis to more realistic systems is provided in App. A and B, which deal with finite (not pinhole) apertures. They result in the following:

Corollary 3: *An illumination point source creates a flare pattern which is symmetric around ℓ^{flare} , if the iris is radially symmetric.*

Proposition 4: *Lens flare caused by secondary reflections contains a dilated version of $\Phi_{\mathcal{C}}$. The dilation around each point in $\Phi_{\mathcal{C}}$ is set by the shape of the iris.*

The latter conclusion theoretically expresses a familiar observation which had prompted the term *aperture ghosting*.

4. Aperture Deghosting

This section presents an estimation of I , from which aperture ghosting is eliminated. As a by-product, images of the aperture ghosts are derived. In Sec. 5, these images are used to extract geometric information.

³Veiling glare is also created by scattering, e.g., from dust or fingerprints on the lens. Our analysis does not deal with this kind of flare, but only with flare associated with reflections from the glass interfaces. This form causes the strong spatial variations characteristic of aperture ghosts.

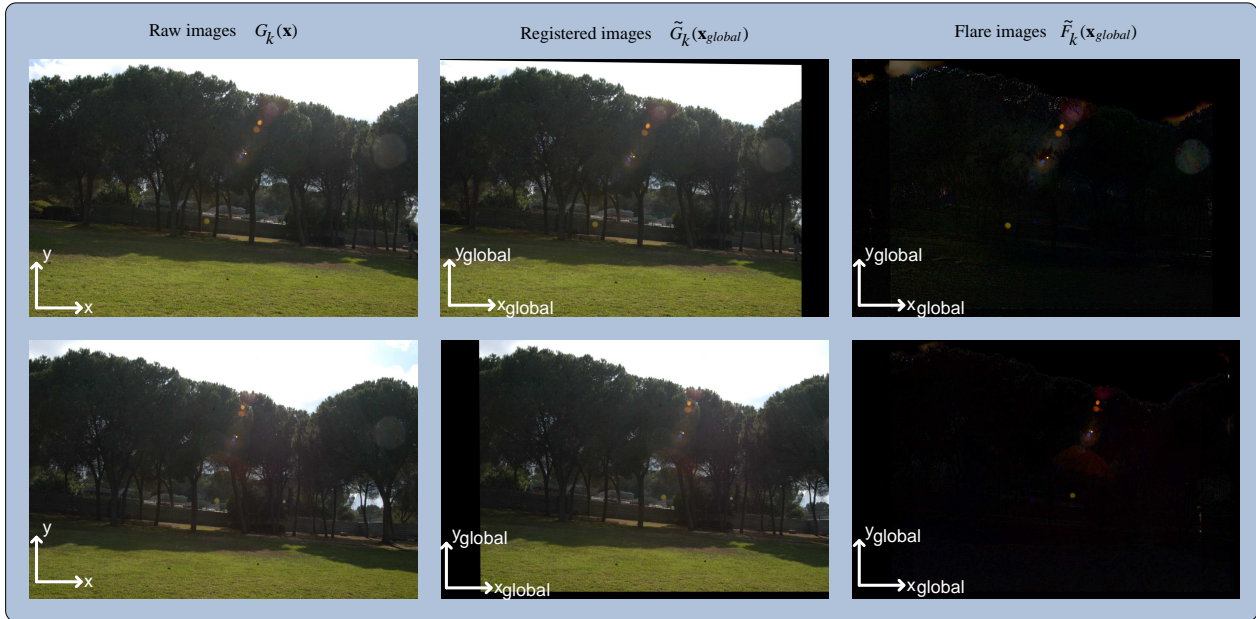


Figure 3. Experiment. [Left] Sample raw frames. [Middle] The corresponding geometrically registered frames. [Right] The resulting estimated flare images, in the global coordinate system. Most of their energy is in spots (aperture ghosts) along a straight line $\tilde{\ell}_k^{\text{flare}}$. However, the real-life system is not going by the perfect model: there is a weak aperture ghost on the right, way off $\tilde{\ell}_k^{\text{flare}}$. In addition, there is some energy elsewhere, caused by slight errors of image alignment. Nevertheless, the algorithms tolerated these imperfections.

4.1. Image Acquisition

Take K_{frames} raw images, each denoted as $G_k(\mathbf{x})$, where $k \in [1, K_{\text{frames}}]$. All of them capture the same scene. Between frames, the camera moves e.g., in an uncontrolled manner, as in hand-held cameras. For example, using a moving Nikon D100 camera outdoors,⁴ we simply acquired a set of three frames from the same point of view. Two of these frames are shown in the left column of Fig. 3.

The light source at \mathbf{X}^{sol} is projected to a different image-plane location $\mathbf{x}_k^{\text{sol}}$ in each frame k , due to camera motion. Thus, following Theorem 1, in each frame k , the flare is concentrated on a different line in the frame's internal coordinate system \mathbf{x} . This line passes through the static \mathbf{o} and the varying $\mathbf{x}_k^{\text{sol}}$. Denote this line as ℓ_k^{flare} .

Since \mathbf{X}^{sol} is typically very far, motion of $\mathbf{x}_k^{\text{sol}}$ is achieved only if the camera motion has a rotation component. The line ℓ_k^{flare} still does not move, if the camera rotation axis is normal to the plane $\mathcal{P}^{\text{meridion}}$. In general, however, such pathological cases are rare: typically, the camera rotates, and not around a particularly degenerate axis.

The subsequent stages require image registration. This is easier to achieve if the camera rotates around $\mathbf{X}^{\text{center}}$, or if the objects are far enough. In this paper, we assume that motion can indeed be compensated for by registration.

4.2. Deghosting the Sequence

Aperture ghosts condense around a line in each frame. In the frames acquired in Sec. 4.1, this line moves. Hence,

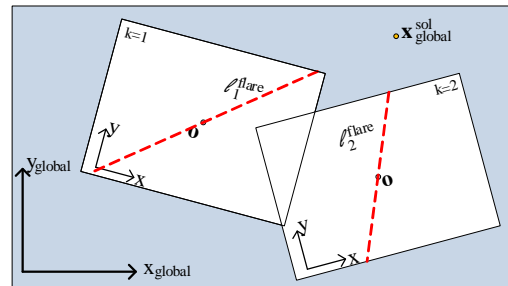


Figure 4. The internal coordinates \mathbf{x} in frame k , are transformed to the global coordinates $\mathbf{x}_{\text{global}}$ via an operator \mathcal{T}_k .

object parts that are overlaid with aperture ghosts in one frame, can generally come out of this flare component in other frames. This is the key for our simple deghosting.

Let us compensate for the scene/camera motion. Any coordinate \mathbf{x} in frame k is transformed to a corresponding point in a global 2D coordinate system $\mathbf{x}_{\text{global}} = (x_{\text{global}}, y_{\text{global}})$, using a registration operator \mathcal{T}_k

$$\mathbf{x}_{\text{global}} = \mathcal{T}_k(\mathbf{x}) , \quad (10)$$

as illustrated in Fig. 4. The registered frames are denoted $\tilde{G}_k(\mathbf{x}_{\text{global}})$. Now, Eq. (2) becomes

$$\tilde{G}_k(\mathbf{x}_{\text{global}}) = I(\mathbf{x}_{\text{global}}) + \tilde{F}_k(\mathbf{x}_{\text{global}}) . \quad (11)$$

The middle column in Fig. 3 shows registered frames $\tilde{G}_k(\mathbf{x}_{\text{global}})$. In Eq. (11), the component $I(\mathbf{x}_{\text{global}})$ is independent of k , since the true scene (without flare) is assumed to be temporally constant in the global system.

⁴The frames were acquired in RAW format to maintain linearity.



Figure 5. A deghosted image, based on data corresponding to Fig. 3.

The component $\tilde{F}_k(\mathbf{x}_{\text{global}})$ changes between the registered frames. Before registration, the flare moves with (and within) the line ℓ_k^{flare} . As described in Sec. 4.1, the motion of the line is different than the apparent motion of the scene within each frame. For this reason, registration which is tuned to the object $I(\mathbf{x}_{\text{global}})$ does not align the flare, as illustrated in Fig. 4. This is similar to the situation of motion of *transparent layers*, as analyzed in Refs. [1, 2, 7, 17, 20, 22].

For each location $\mathbf{x}_{\text{global}}$ in the captured FOV there is a set of frames that acquire measurements at this global coordinate. Denote this set of frame-indices as $\Omega(\mathbf{x}_{\text{global}})$. Now, recall that the flare $\tilde{F}_k(\mathbf{x}_{\text{global}})$ is always *non-negative*. Hence, we use a simple deflaring estimator

$$\hat{I}(\mathbf{x}_{\text{global}}) = \min_{k \in \Omega(\mathbf{x}_{\text{global}})} \tilde{G}_k(\mathbf{x}_{\text{global}}) . \quad (12)$$

Fig. 5 shows the result of this operation, based on the experimental data shown in Fig. 3. Indeed, the aperture ghosts are effectively eliminated.

Note that $\hat{I}(\mathbf{x}_{\text{global}})$ is an *upper bound* for $I(\mathbf{x}_{\text{global}})$. Flare may exist at $\mathbf{x}_{\text{global}}$ even in the dimmest measurement. However, aperture ghosts are rather *localized* with significantly lower flare intensity outside the aperture ghosts. Thus, Eq. (12) is effective in eliminating this component.

In Ref. [17], an operation similar to Eq. (12) was used in the context of window semi-reflections. However, the favorable *locality* of ghosting is usually not the case in window semi-reflections [1, 2, 7, 17, 20, 22]. In a window, the disturbing spatially varying reflection may cover the whole FOV. There, the minimization (Eq. 12) may not suffice if the motion of the reflected layer is not long enough, but in aperture ghosting just a small motion⁵ usually suffices. Consequently, the deghosting shown in Figs. 3,5 is successfully achieved also with $K_{\text{frames}} = 2$, experimentally.

As a by-product, an estimate of the set of aperture-ghosting images is derived by

$$\hat{\tilde{F}}_k(\mathbf{x}_{\text{global}}) = \tilde{G}_k(\mathbf{x}_{\text{global}}) - \hat{I}(\mathbf{x}_{\text{global}}) . \quad (13)$$

⁵Too small motion may maintain residual overlap between aperture ghosts in different frames $\tilde{G}_k(\mathbf{x}_{\text{global}})$. Then, gradient-domain approaches [23] can be helpful.

The right column in Fig. 3 shows the resulting flare images $\hat{\tilde{F}}_k(\mathbf{x}_{\text{global}})$ in the experiment.

5. Geometry from Flare

Theorem 1 states a constraint about flare, which involves two points: the location of the light-source’s projection, and the optical center of a frame. In this section, we exploit this constraint in order to estimate these two points.

5.1. Where is the Sun?

The light source from which flare originates (associated here with the Sun⁶) is at a fixed 3D position \mathbf{X}^{sol} . In the global coordinate system, the Sun’s projection is at $\mathbf{x}_{\text{global}}^{\text{sol}}$, common to all registered frames. However, $\mathbf{x}_{\text{global}}^{\text{sol}}$ is often outside the camera FOV. Otherwise, it may saturate the camera, or induce underexposure of the rest of the scene. Now, we describe a way to recover $\mathbf{x}_{\text{global}}^{\text{sol}}$, even-though the Sun may not be visible in the images.

5.1.1 Principle

“There has to be an invisible sun.”

- Sting & The Police

The registered flare images $\hat{\tilde{F}}_k(\mathbf{x}_{\text{global}})$ were derived in Eq. (13). Each of them condenses around a line $\tilde{\ell}_k^{\text{flare}}$. This line is equivalent to the unregistered line ℓ_k^{flare} , yet rectified to the global coordinate system $\mathbf{x}_{\text{global}}$. Following Theorem 1, each such line must pass through the projection of the Sun. Hence, $\tilde{\ell}_k^{\text{flare}}$ must pass through $\mathbf{x}_{\text{global}}^{\text{sol}}$. This is illustrated in Fig. 4.

As the images are registered, their internal coordinates are transformed by Eq. (10). Hence, any central pixel \mathbf{o} is transferred to location $\tilde{\mathbf{o}}_k = \mathcal{T}_k(\mathbf{o})$. These locations are generally different and not co-linear with $\mathbf{x}_{\text{global}}^{\text{sol}}$, as seen in Fig. 4. Consequently, $\mathbf{x}_{\text{global}}^{\text{sol}}$ can be found as the *intersection of the lines* $\tilde{\ell}_k^{\text{flare}}$, *in the global coordinate system*.

5.1.2 Low Level Estimator of the Sun’s Location

We avoid explicit implementation of the description in Sec. 5.1.1, which might apparently involve detection of features such as edges or hexagonal ghosts, line detection and then least-squares estimation of intersection by multiple lines. We preferred a simple low-level approach which involves no feature extraction. The approach seeks the point $\mathbf{x}_{\text{global}}^{\text{sol}}$, which is most consistent with the whole data.

Let \mathbf{a} be a coordinate column vector in an arbitrary spatial domain. A line in the \mathbf{a} plane is parameterized by a vector $\mathbf{l} = (r, \theta)$. Here, $\theta \in [0, \pi]$ is the angle of a normal to the line (See Fig 6a), and r is the signed displacement the line from the origin of the \mathbf{a} coordinate system. The Radon transform of a function $h(\mathbf{a})$ is defined as

⁶Ref. [16] studied the distribution of the Sun’s location in art.

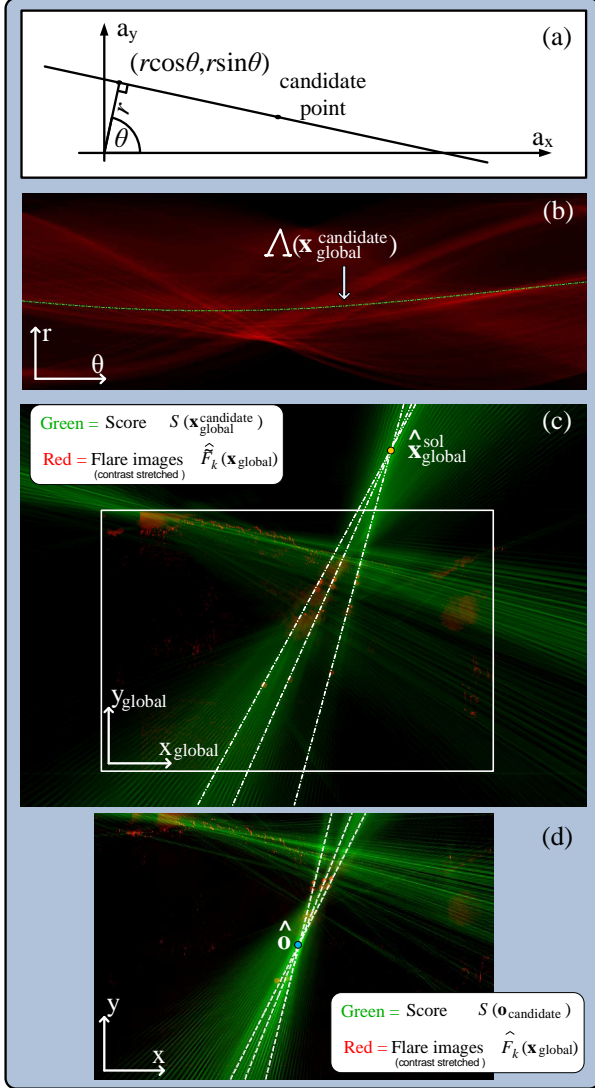


Figure 6. (a) Polar representation of a line in an arbitrary coordinate plane \mathbf{a} . (b) Radon transform of one of the estimated flare images. [Green curve]: a set Λ of lines \mathbf{l} that pass through a candidate point. (c) Estimation of the solar location $\hat{\mathbf{x}}_{\text{global}}^{\text{sol}}$. Dashed marked lines maximize Eq. (16) per frame. (d) Estimation of the optical center \mathbf{o} . Dashed marked lines maximize Eq. (19).

$$\mathcal{R}_1\{h(\mathbf{a})\} = \iint h(\mathbf{a}) \delta \left(r - \left[\begin{array}{c} \cos \theta \\ \sin \theta \end{array} \right]^t \mathbf{a} \right) d\mathbf{a}, \quad (14)$$

where t denotes transposition and δ is Dirac's delta function. Now, take the estimated flare images derived by Eq. (13), and apply the Radon transform (14) on each of them. Here, we set $\mathbf{a} = \mathbf{x}_{\text{global}}$, and $h = \hat{F}_k(\mathbf{x}_{\text{global}})$. The result is $\mathcal{R}_1\{\hat{F}_k(\mathbf{x}_{\text{global}})\}$. A high value of this function indicates a high score for an intense line parameterized with (r, θ) , in flare-image k (See Fig. 6b).

Let a candidate position for the Sun's projection be at $\mathbf{x}_{\text{global}}^{\text{candidate}}$. Similarly to Fig. 6a, any line that passes through

this point should satisfy

$$r = [\cos \theta \ \sin \theta] \mathbf{x}_{\text{global}}^{\text{candidate}}, \quad (15)$$

where $\mathbf{x}_{\text{global}}^{\text{candidate}}$ is a column vector. For each θ there is a unique r that satisfies Eq. (15). Hence, a specific $\mathbf{x}_{\text{global}}^{\text{candidate}}$ defines a set of vectors $\mathbf{l} = (r, \theta)$. This set describes all possible straight lines passing through this point as plotted in Fig. 6b. Denote this set of lines as $\Lambda(\mathbf{x}_{\text{global}}^{\text{candidate}})$.

Now, instead of scoring a line, as in Eq. (14), we score a candidate solar point $\mathbf{x}_{\text{global}}^{\text{candidate}}$: in a single flare-image k ,

$$s_k(\mathbf{x}_{\text{global}}^{\text{candidate}}) = \max_{\mathbf{l} \in \Lambda(\mathbf{x}_{\text{global}}^{\text{candidate}})} \mathcal{R}_1 \left\{ \hat{F}_k(\mathbf{x}_{\text{global}}) \right\}. \quad (16)$$

A high score $s_k(\mathbf{x}_{\text{global}}^{\text{candidate}})$ means that through $\mathbf{x}_{\text{global}}^{\text{candidate}}$ passes an intense line (for which the line-ranking $\mathcal{R}_1\{\hat{F}_k(\mathbf{x}_{\text{global}})\}$ is high) in flare-image k . Based on this, the total score for a candidate point is

$$S(\mathbf{x}_{\text{global}}^{\text{candidate}}) = \sum_{k=1}^{K_{\text{frames}}} s_k(\mathbf{x}_{\text{global}}^{\text{candidate}}). \quad (17)$$

The best ranking candidate is the estimated solar projection:

$$\hat{\mathbf{x}}_{\text{global}}^{\text{sol}} = \arg \max_{\mathbf{x}_{\text{global}}^{\text{candidate}}} S(\mathbf{x}_{\text{global}}^{\text{candidate}}). \quad (18)$$

Lines passing through $\hat{\mathbf{x}}_{\text{global}}^{\text{sol}}$ have the most accumulated energy.

The result that corresponds to the data described in Fig. 3 is shown in Fig. 6c. The function $S(\mathbf{x}_{\text{global}}^{\text{candidate}})$ is in green. The selected point $\hat{\mathbf{x}}_{\text{global}}^{\text{sol}}$ resulting from Eq. (18) is shown, as well as the lines \mathbf{l} , that maximize the score in each frame (Eq. 16). By definition, they all intersect at $\hat{\mathbf{x}}_{\text{global}}^{\text{sol}}$. Overlaid in red are three registered flare images \hat{F}_k .

5.2. Where is the Optical Axis?

Due to hardware misalignment the OA may not intersect the image plane at the frame's center. Here \mathbf{o} is estimated as a by-product of deflaring. According to Sec. 4.1, flare is condensed around a line ℓ_k^{flare} in each raw (unregistered) frame k . Following Theorem 1, each such line passes through \mathbf{o} . Thus, \mathbf{o} can be found as the *intersection of ℓ_k^{flare} , in the internal coordinate system \mathbf{x} of the frames.*

Estimation of \mathbf{o} can be done in a manner analogous to Sec. 5.1.2. Take the flare images derived by Eq. (13). Then, invert the registration (Eq. 10): a flare value in a pixel of the image $\hat{F}_k(\mathbf{x}_{\text{global}})$ is assigned to a pixel $\mathbf{x} = \mathcal{T}_k^{-1}(\mathbf{x}_{\text{global}})$ in frame k . This yields flare images $\hat{F}_k(\mathbf{x})$, which geometrically correspond to the raw unregistered frames.

Now we set $\mathbf{a} = \mathbf{x}$ and $h = \hat{F}_k(\mathbf{x})$, and apply the Radon transform (14), in analogy to Sec. 5.1.2. The result is $\mathcal{R}_1\{\hat{F}_k(\mathbf{x})\}$. Let a candidate position for \mathbf{o} be at $\mathbf{o}^{\text{candidate}}$, which defines a set $\Lambda(\mathbf{o}^{\text{candidate}})$ of lines passing through it. In analogy to Eqs. (16,17), the score for the candidate is

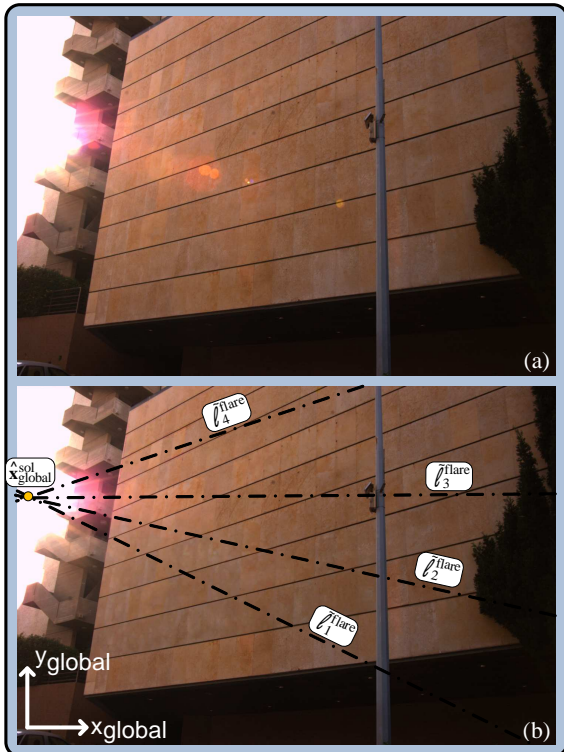


Figure 7. (a) A raw frame. (b) The deghosted image. The marked lines maximize Eq. (16) per frame, and correspond to $\tilde{\ell}_k^{\text{flare}}$ in the global system. Their intersection is the Sun's location.

$$S(\mathbf{o}^{\text{candidate}}) = \sum_{k=1}^{K_{\text{frames}}} \max_{\mathbf{l} \in \Lambda(\mathbf{o}^{\text{candidate}})} \mathcal{R}_1 \left\{ \hat{F}_k(\mathbf{x}) \right\}. \quad (19)$$

The candidate that maximizes $S(\mathbf{o}^{\text{candidate}})$ is the estimation of \mathbf{o} , denoted $\hat{\mathbf{o}}$.

The result that corresponds to the data of Fig. 3 is shown in Fig. 6d. The function $S(\mathbf{o}^{\text{candidate}})$ is in green. The point $\hat{\mathbf{o}}$ is shown, as well as the lines \mathbf{l} that maximize the score. Three unregistered flare images \hat{F}_k are overlaid in red.

6. Selective Processing

Deghosting as in Eq. (12) can be more efficient, by applying it only to pixels around ℓ_k^{flare} . Other pixels in frame k are unaffected by ghosting, and need no processing. Such a mode can help processing of dynamic scenes, since most of the FOV maintains the raw moving information, and only the regions of ℓ_k^{flare} are temporally processed.

Such a selective processing is demonstrated in an experiment. Fig. 7a shows a sample raw frame. The Sun is in the FOV, but it saturates and blooms the area around \mathbf{x}^{sol} . Hence, the Sun is not visible. The area adjacent to the Sun exhibits a glare type which is not aperture-ghosting, since it contains thin lines not directed to the frame's center. Such a glare component is not dealt with in our method. Nevertheless, the acquired images suffered from significant aperture ghosting, which affects areas distant from \mathbf{x}^{sol} .

The data was processed first using Eqs. (12,13,16,17,18). This yielded the estimated $\mathbf{x}_{\text{global}}^{\text{sol}}$, as well as the lines in $\Lambda(\mathbf{x}_{\text{global}}^{\text{sol}})$ which maximized Eq. (16), per frame. The latter are associated with $\tilde{\ell}_k^{\text{flare}}$. Finally, Eq. (12) was re-applied to the data, this time only in a band around $\tilde{\ell}_2^{\text{flare}}$. The rest of \hat{I} was simply pasted from the registered frame \hat{G}_2 . The result is shown in Fig. 7b.

7. Discussion

Useful results can also be extracted if the camera is static, but the light source moves. This occurs naturally outdoors, due to the Sun's trajectory. Then, ℓ^{flare} changes its orientation in time. The orientation and its kinetics depend on the camera's viewing direction relative to the south (in the northern terrestrial hemisphere). This provides cues that may complement Ref. [10] as a visual compass.

In artificial lighting, ghosting can be caused by multiple illumination sources. In each raw frame, multiple flare lines ℓ^{flare} exist, all passing through \mathbf{o} . We expect Eq. (12) to work there as well, perhaps requiring more frames. Finding the locations $\hat{\mathbf{x}}_{\text{global}}^{\text{sol}}$ of the multiple sources is more involved, and may require turning Eq. (18) from an expression of a single-maximum to a clustering formulation.

Flare also occurs in other sensing modalities. For instance, in thermal imaging, radiation from hot sources and the camera interior are diverted and reflected [3] by the optics towards pixels. It may be possible to deflare such measurements using a method similar to the one presented here.

The geometric model in the paper assumes that the optical elements share the same OA. Deviations from this assumption are caused by slight unintended misalignment of elements, which may be the reason for the off- ℓ^{flare} ghost in Fig. 3. In some systems, some elements are necessarily radially asymmetric, such as prisms (used in optical image stabilization). The impact of these deviations on the geometric estimation of \mathbf{x}^{sol} is yet to be studied. Nevertheless, the photometric model (Sec. 3.1) is valid even under deviation from radial symmetry. Hence, aperture deghosting as described in Sec. 4 is resistant to such deviations.

A. Ghosting by a Finite-Aperture

The chief ray creates flare at a set of points Φ_C , which lies on ℓ^{flare} (Theorem 1). The aperture has a finite size, hence allowing into the lens rays from \mathbf{X}^{sol} that are not-chief. How does this affect the flare?

Let \mathbf{u} be a point in the entrance pupil, as illustrated in Fig. 8. A ray $\mathcal{L}(\mathbf{u})$ is emitted from \mathbf{X}^{sol} . It passes through \mathbf{u} in the entrance pupil, slightly deviating from the chief ray. The ray \mathcal{L} refracts through the lens system, and eventually it projects onto \mathbf{x}^{sol} on $\mathcal{P}^{\text{sensor}}$ (if the focus settings are tuned to the distance of \mathbf{X}^{sol}). On its way, $\mathcal{L}(\mathbf{u})$ yields a set of internally reflected rays $\{\tilde{\mathcal{L}}_q(\mathbf{u})\}_{q=1}^{N_{\text{secondary}}}$. The parameters (location and direction) of each secondary ray $\tilde{\mathcal{L}}_q(\mathbf{u})$

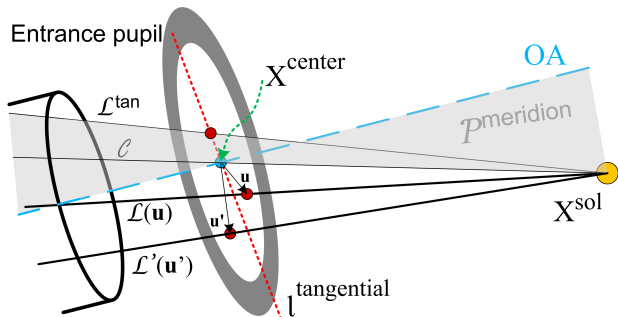


Figure 8. The entrance pupil is bisected by $\mathcal{P}^{\text{meridion}}$ at line $\ell^{\text{tangential}}$. A tangential ray \mathcal{L}^{tan} is in $\mathcal{P}^{\text{meridion}}$. Rays $\mathcal{L}(\mathbf{u})$ and $\mathcal{L}'(\mathbf{u}')$ pass at symmetric points relative to $\ell^{\text{tangential}}$, and follow symmetric trajectories.

are smooth functions of \mathbf{u} . The reason is that the laws of specular reflection (e.g., outgoing angle equals the incident angle) are smooth, and the lens surfaces are smooth as well.

Consequently, the intersection of $\tilde{\mathcal{L}}_q(\mathbf{u})$ with $\mathcal{P}^{\text{sensor}}$ is a smooth function at a small \mathbf{u} . Hence, if \mathcal{L} infinitesimally deviates from the chief ray \mathcal{C} , then the flare caused by \mathcal{L} would deviate infinitesimally from $\Phi_{\mathcal{C}}$. As a consequence, aperture ghosts are mostly a dilated version of $\Phi_{\mathcal{C}}$, where the dilation around each point in $\Phi_{\mathcal{C}}$ is continuous.

The deviation \mathbf{u} is bounded by the entrance pupil [6], which has the shape of the lens iris. Hence, the shape of this pupil bounds the deviation of the flare from $\Phi_{\mathcal{C}}$. The entrance pupil has the shape of the iris (it is an image of the iris [6]). Thus, the iris shape sets the image domain of finite-aperture ghosting, leading to Proposition 4 in Sec. 3.2.

B. Symmetry

Approximate the entrance pupil by a circle. Then, as discussed here, ℓ^{flare} is an axis of reflection symmetry for finite-aperture flare. Consider Fig. 8. The entrance-pupil is intersected by $\mathcal{P}^{\text{meridion}}$ at a line $\ell^{\text{tangential}}$. Since $X^{\text{center}} \in \ell^{\text{tangential}}$, the symmetric pupil is bisected by $\ell^{\text{tangential}}$. Thus, for any position \mathbf{u} in the pupil, there is a reflected position \mathbf{u}' (with respect to $\ell^{\text{tangential}}$) in the pupil.

Now, consider a flare point outside ℓ^{flare} . It is created by internally reflected rays, which stem from a non-chief ray $\mathcal{L}(\mathbf{u})$. There is thus another ray $\mathcal{L}'(\mathbf{u}')$ which passes through the symmetric position \mathbf{u}' in the entrance pupil. By symmetry considerations, it creates a reflected flare around ℓ^{flare} . This yields Corollary 3 in Sec. 3.2.

Acknowledgments

We thank Aryeh Weiss and Michael Elad for useful discussions, and Paul van Walree for permitting the use of Fig. 1. Yoav Schechner is a Landau Fellow - supported by the Taub Foundation. This work was supported by the Israeli Ministry of Science, Culture and Sport (Grant 3-3426). It was conducted in the Ollendorff Minerva Center. Minerva is funded through the BMBF.

References

- [1] E. Beery and A. Yeredor. Blind separation of superimposed shifted images using parameterized joint diagonalization. *IEEE Trans. Image Proc.*, 17:340–353, 2008. 5
- [2] J. R. Bergen, P. J. Burt, R. Hingorani, and S. Peleg. A three-frame algorithm for estimating two component image motion. *IEEE Trans. PAMI*, 14:886–895, 1992. 5
- [3] S. Bobrov and Y. Y. Schechner. Image-based prediction of imaging and vision performance. *JOSA-A*, 24:1920–1929, 2007. 7
- [4] Y. Diamant and Y. Y. Schechner. Overcoming visual reverberations. In *Proc. IEEE CVPR*, 2008. 2
- [5] J. A. Ferwerda, S. N. Pattanaik, P. Shirley, and D. P. Greenberg. A model of visual adaptation for realistic image synthesis. In *Proc. Comp. Graphics & Interactive Tech.*, pages 249–258, 1996. 2
- [6] E. Hecht. *Optics*, chapter 6. Addison Wesley, 4th edition, 2001. 2, 8
- [7] M. Irani, B. Rousso, and S. Peleg. Computing occluding and transparent motions. *Int. J. Comp. Vis.*, 12:5–16, 1994. 5
- [8] J. Knoll, *Knoll Light Factory*, Red Giant Software. 1
- [9] G. Kuwabara. On the flare of lenses. *JOSA*, 11:1850–1856, 1953. 1
- [10] J. Lalonde, S. G. Narasimhan, and A. A. Efros. What does the sky tell us about the camera? In *Proc. ECCV*, 2008. 7
- [11] *The Newport Resource 2006-2007*, pages 509–510. 2
- [12] R. Raskar, A. Agrawal, C. Wilson, and A. Veeraraghavan. Glare aware photography: 4D ray sampling for reducing glare effects of camera lenses. *ACM TOG*, 27, 2008. 1
- [13] S. F. Ray. *Applied Photographic Optics*, chapter 15. Focal Press, 2nd edition, 1994. 1, 2
- [14] S. Seitz, Y. Matsushita, and K. Kutulakos. A theory of inverse light transport. In *IEEE ICCV*, volume 2, pages 1440–1447, 2005. 2
- [15] W. Smith. *Modern Optical Engineering*, chapter 6. McGraw-Hill, 3rd edition, 2000. 1, 2
- [16] J. Sun and P. Perona. Where is the sun? *Nature Neuroscience*, 1:183–184, 1998. 5
- [17] R. Szeliski, S. Avidan, and P. Anandan. Layer extraction from multiple images containing reflections and transparency. *Proc. IEEE CVPR*, 1:246–253, 2000. 5
- [18] E. Talvala, A. Adams, M. Horowitz, and M. Levoy. Veiling glare in high dynamic range imaging. *ACM TOG*, 26, 2007. 1, 2
- [19] T. Treibitz and Y. Y. Schechner. Recovery limits in pointwise degradation. In *Proc. IEEE ICCP*, 2009. 1
- [20] Y. Tsin, S. B. Kang, and R. Szeliski. Stereo matching with linear superposition of layers. *IEEE Trans. PAMI*, 28:290–301, 2006. 5
- [21] P. van Walree. <http://www.vanwalree.com/optics.html>. 1
- [22] J. Wang and E. Adelson. Layered representation for motion analysis. In *Proc. IEEE CVPR*, pages 361–365, 1993. 5
- [23] Y. Weiss. Deriving intrinsic images from image sequences. In *Proc. IEEE ICCV*, vol. 2, pages 68–75, 2001. 5
- [24] F. Xiao, J. M. DiCarlo, P. B. Catrysse, and B. A. Wandell. High dynamic range imaging of natural scenes. In *Proc. Color Imaging Conf.*, pages 337–342, 2002. 1